Surface Reconstruction from Point Clouds by Transforming the Medial Scaffold

Ming-Ching Chang
LEMS, Engineering
Brown University, USA
mcchang@lems.brown.edu

Frederic F. Leymarie
Goldsmiths College
University of London, UK
ffl@gold.ac.uk

Benjamin B. Kimia
LEMS, Engineering
Brown University, USA
kimia@lems.brown.edu

Abstract

We propose an algorithm for surface reconstruction from unorganized points *based on a view of the sampling process as a deformation from the original surface. In the course of this deformation the* Medial Scaffold *($\mathcal{MS}$) — a graph representation of the 3D* Medial Axis *($\mathcal{MA}$) — of the original surface undergoes abrupt changes (transitions) such that the $\mathcal{MS}$ of the unorganized point set is significantly different from that of the original surface. The algorithm seeks a sequence of transformations of the $\mathcal{MS}$ to invert this process. Specifically, some $\mathcal{MS}$ curves (junctions of 3 $\mathcal{MA}$ sheets) correspond to triplets of points on the surface and represent candidates for generating a (Delaunay) triangle to mesh that portion of the surface. We devise a greedy algorithm that iteratively transforms the $\mathcal{MS}$ by "removing" suitable candidate $\mathcal{MS}$ curves (gap transform) from a rank-ordered list sorted by a combination of properties of the $\mathcal{MS}$ curve and its neighborhood context. This approach is general and applicable to surfaces which are: non-closed, non-orientable, non-uniformly sampled. In addition, the method is comparable in speed and complexity to current popular Voronoi/Delaunay-based algorithms, and is applicable to very large datasets.*

1. Introduction

We consider the problem of constructing surface meshes from a sampling in the form of an *unorganized cloud of points*. The recovery of this connectivity amongst points is typically based on assuming *(i)* some surface continuity, possible smoothness, and *(ii)* sufficient sampling density to capture all surface features.

Our approach is meant to be general and applicable to various topologies (Fig.2); in particular it does not assume that the surfaces are smooth, nor closed, nor orientable, it does not require uniform sampling, it can handle varying noise levels, and it is scalable to arbitrarily large input datasets (Fig.1), as discussed below.

Our approach is based on the notion of representing shape via deformations and their local, successive topologi-

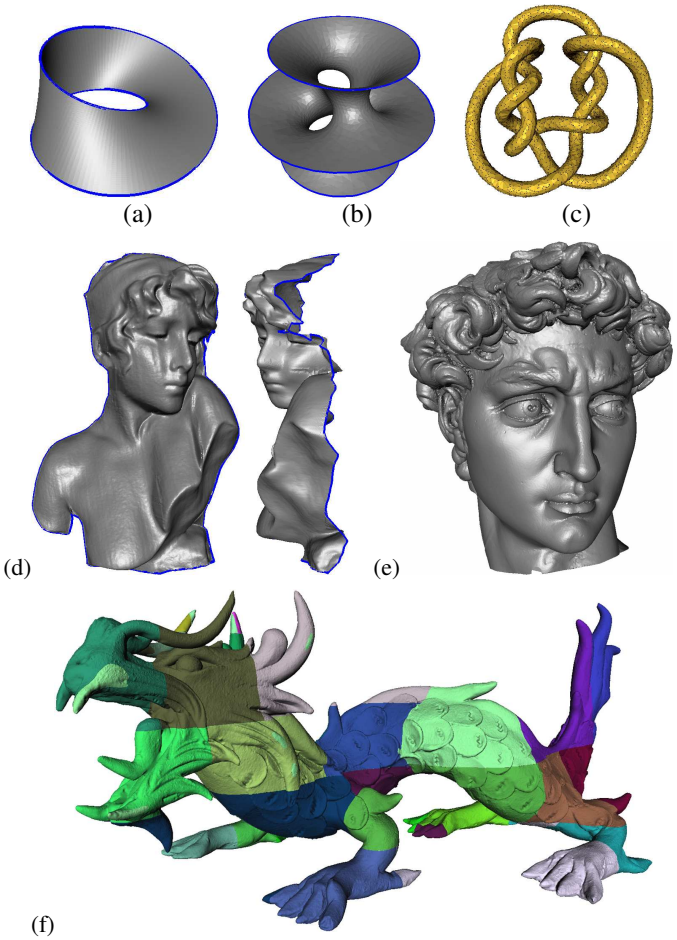

Figure 1. Surface reconstruction from *unorganized* point clouds, using $\mathcal{MS}$ transformations, of several topology types: (a) Moebius strip (non-orientable), (b) Costa's minimal surface, with the topology of a torus thrice punctured, (c) Connected water-tight knot (highly non-uniform sampling of 10K points), (d) a complex surface with recovered boundary (in blue): the Sapho raw scan dataset (121K points, Stony Brook), (e) Michelangelo's David head (250K points, Stanford), (f) the combination of several reconstruction results (in various colors) from a 3D bucketing and stitching of the Stanford Asian Dragon dataset ($\approx 3,6 \times 10^6$ points).

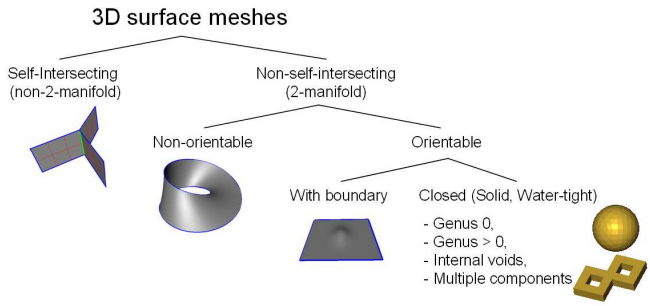

Figure 2. Classification of surfaces based on topology.

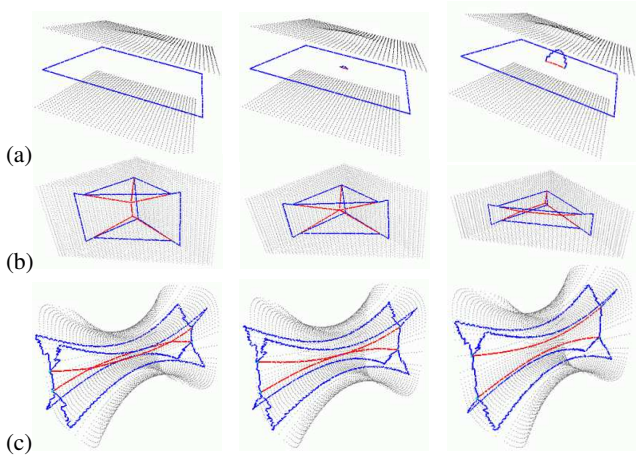

Figure 3. Illustration of some $\mathcal{MS}$ (or $\mathcal{MA}$) *transitions* in 3D. The (a) $A_1A_3 - I$, (b) A_1^5, and (c) A_1^4 transitions; details in [13].

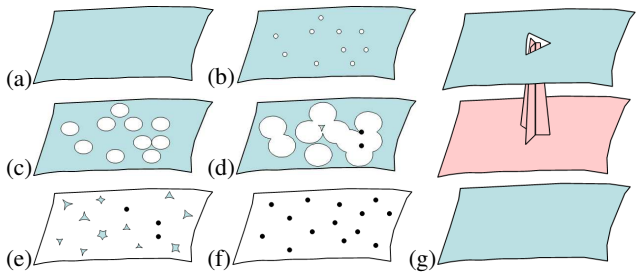

Figure 4. This figure illustrates that "sampling" a surface to produce an unorganized cloud of points can be viewed as a *deformation process*: (a) the original surface; (b) some points are taken away from the surface, creating holes; (c) these holes grow thus reducing the area of the remaining surface patch, and (d) eventually start joining to form larger gaps and isolated patches; (e) the remaining surface patches each tend to shrink to a point; (f) the resulting point cloud represents samples of the surface. (g) An infinitesimal but generic hole creates three $\mathcal{MA}$ sheets with a common A_1^3 curve.

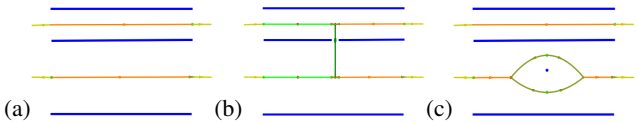

Figure 5. (a) The dark blue curves are 2D object contour segments and other colors represent shocks. (b) The removal of an object point adds a line to the shock graph, while (c) adding a point creates a loop; we are only concerned with the former process in this paper.

cal variations. It is directly inspired from previous work by Kimia *et al.* in 2D and 3D [18, 28, 13, 26, 14] who represent shape as a member of an equivalence class, each defined as the set of shapes sharing a common shock graph topology: "shocks" are simply the Medial Axis ($\mathcal{MA}$) points endowed with a sense of dynamics of flow which arises when the $\mathcal{MA}$ is considered as the quench points of a propagating "grass fire" from the contour samples. In 2D the shock graph is a planar directed graph while in 3D the classification of shocks into five types, namely two types of vertices, two types of curves, and one type of sheet, first gives rise to a *hypergraph*, referred to as the *Augmented Medial Scaffold* ($\mathcal{MS}^+$) which explicitly retains the topology of $\mathcal{MA}$ vertices, curves, and sheets, and second to a 3D directed graph, the *Medial Scaffold* ($\mathcal{MS}$) which explicitly retains the topology of $\mathcal{MA}$ vertices and curves, while $\mathcal{MA}$ sheets are implicitly represented as loops in the graph [19]. All 3D shapes sharing the same $\mathcal{MS}$ are equivalent.

In addition to defining an equivalence class of shapes, which effectively reduces the dimensionality of the "shape space," an equivalence class of deformation paths is also needed. Observe that the $\mathcal{MS}$ (equivalently the $\mathcal{MA}$) undergoes abrupt changes or *transitions*, as the shape is deformed, Fig.3. Two deformation paths sharing the same sequence of transitions are similar and thus are considered to be equivalent. This equivalence class of deformations acting on an equivalence class of shapes effectively *discretizes the shape space*.

Our approach can now be described in the above context: *complete surfaces and sampled surfaces are simply two points in the shape space that are closely related*. In an approach to 2D object recognition, [26] found the optimal deformation path between two shapes and used its cost to establish similarity between them, leading to a highly successful object recognition scheme. In an approach to 2D perceptual grouping, [30] used a greedy approach to find more regular shapes from unorganized data. Similarly, in our case, a sampled shape is simply a deformation of the original surface, as illustrated in Fig.4. In this process, the $\mathcal{MS}$ undergoes abrupt transitions (topological events). Fig.5 shows the transitions for deforming curves in 2D by removing or adding points.

The process of achieving a transition on an existing

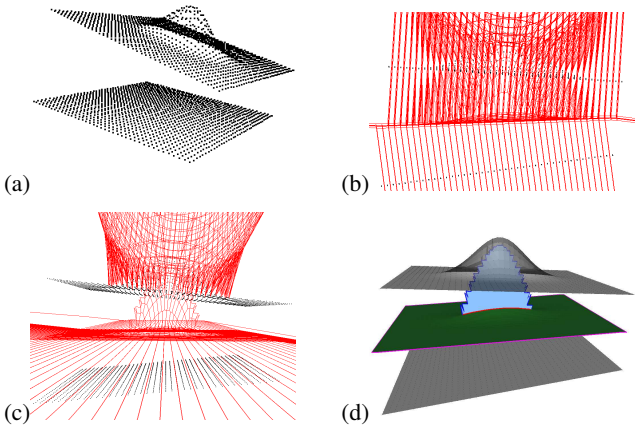

Figure 6. Illustration of the proposed *shock segregation* process. (a) A set of 3,200 points are uniformly distributed on a pair of planes, one of which is deformed by an elongated Gaussian kernel; (b) side-view of the corresponding $\mathcal{MS}$. (c) The remaining scaffold after undergoing a series of *3D gap transforms*. (d) The results of this shock segregation are two-fold: *(i)* the reconstructed surface and *(ii)* its corresponding $\mathcal{MS}^+$.

shape is called a *symmetry transform*, *i.e.*, by changing the $\mathcal{MS}$ we are jointly deforming the shape. Ideally, all sequences of transitions should be considered, *i.e.*, the ones described in Fig.3 and additional ones having to do with adding and removing isolated points. In this paper, however, we restrict ourselves only to the transition arising from removing a patch from the surface (the first step in our view of the sampling process) and consider only the symmetry transform pertaining to that, called the *gap transform*. Specifically, removing a surface patch, generically results in adding to the $\mathcal{MS}$ a group of three $\mathcal{MA}$ sheets and one $\mathcal{MA}$ curve at their intersection. Thus, the inverse process of reconstructing a surface patch corresponds to consider the removal of such curves and their attached sheets (delimited by loops) from the $\mathcal{MS}$.

As in perceptual grouping in 2D [30], the gap transform in 3D is considered in a greedy sequence, proceeding first with the least cost transform. This cost is based on the likelihood that a $\mathcal{MS}$ curve represents a "missing" surface patch, as well as on the local context (*i.e.*, other reconstructed surface patches which may already exist in the vicinity). Fig.6 illustrates this process on a pair of planar sheets, one of which is somewhat protruding, Fig.6.(a). The $\mathcal{MS}$ (Fig.6.(b)), after a sequence of gap transforms, then resembles that of the original two complete un-sampled surfaces, Fig.6.(c). This in turn enforces a connectivity of the surface samples thus creating a mesh, Fig.6.(d).

The remaining of this paper is organized as follows. We first review the background for surface reconstruction below (§2). We then describe our approach in greater detail (§3), followed by experimental results (§4) and conclusions.

2. Background

Surface reconstruction methods related to our approach can be classified into three main categories, depending if they are based on (1) implicit (distance) functions, (2) propagation (region growing methods), and (3) Voronoi/Delaunay geometric constructs.[1]

Implicit methods can be classified into two subcategories: *(i)* local approximants to the global distance function constructed by blending primitives (implicit functions), and *(ii)* global approximants to the distance function constructed by (volume) propagation. First, *local approximants* mainly differ in three ways: how clusters are generated, the type of implicit function used, and how local functions are blended together. Most recent papers evolve from Blinn's original work [6] and vary mainly in the types of local implicit functions used, *e.g.*, linear combination of Gaussian blobs [22], bounded polynomial in three variables [29], blended union of spheres [20], and, more recently, mixtures of globally supported radial basis functions (RBF's) [8], as well as blended compactly supported RBF's [25]. A line of recent improvements is the multi-level partition of unity implicits (MPU's) [23].

Second, *global approximants* explicitly build a distance field on a grid which tessellates a volume containing the input dataset. Following the early work of Hoppe *et al.* [16], Curless & Levoy meshed range scans by volumetric integration using "lines of sight" [10]. More recent work is based on the level-set methods [32]. Closely related is the method of having an active surface model deform and be attracted towards sample points or data under the influence of a global distance function [31, 27].

Propagation-based methods can be traced back to the algorithm of Boissonnat [7], where a seed edge is picked to find a triangle in the locally estimated tangent plane. More recently, the *ball pivoting algorithm* [5] "rolls a ball" of fixed (parametric) size to reconstruct a mesh, leaving holes in the mesh, a function of the radius parameter which may be iteratively increased to handle non-uniform sampling (but then, risks introducing additional, unwanted interpolants). [17] use the k-nearest-neighboring points to restrict a propagation, and automatically and locally vary the "radius" parameter. Another related alternative is the Intrinsic Property Driven (IPD) algorithm [21], based on the ratio of the lengths of the longest and shortest edges incident to a point. These methods still suffer from topological errors, in particular when two distinct surface patches come close to each other. Gopi *et al.* introduce further restrictive assumptions to help with local ambiguities [15]: locally uniform sampling is assumed, minimum distance between

[1] Other classification schemes have been proposed; *e.g.*, the addition of "hybrid" methods combining the main features of two or more categories.

samples part of different surface patches is set, and smoothness of the original surface is imposed. An important set of propagation-based algorithms uses Delaunay triangles in their scheme; we consider some of these below.[2]

Voronoi/Delaunay methods can be organised in two subcategories, wether they are surface or volume oriented. First, *incremental surface-oriented* methods select suitable Delaunay triangles interpolating sample points either in a batch or in a greedy incremental fashion. A popular recent set of such methods was initiated by the works of Amenta *et al.* who proposed a Voronoi filtering method [1] where they first consider furthest apart Voronoi vertices of a Voronoi cell of a sample point p to define *poles* by pairs, this to approximate the local surface normal. They also define the *local feature size* as the minimum distance from a sample p to the *theoretical* $\mathcal{MA}$ (for a smooth surface with bounded curvatures), which is used to derive theoretical constraints on the sampling and guarantees on the resulting meshes. This was further refined by defining a local neighborhood in the vicinity of a sample p taken as the complement to a cone intersection with its Voronoi cell, called "co-cone," giving a heuristic to approximate the local tangent space at p to restrict the search for neighboring sample to create candidate triangle interpolants [3]. Petitjean and Boyer proposed another approach by defining a notion of r-regularity measured from the samples alone and combined with a discrete (rather than theoretical) $\mathcal{MA}$ [24]. A surface mesh is then constructed by a propagation scheme by selecting Delaunay faces meeting the r-regularity criterion. More recently, Cohen-Steiner and Da have proposed a greedy incremental algorithm that uses for its main heuristic in selecting interpolants the dihedral angle between Delaunay face pairs, which postpones difficult decisions on a queue, and uses additional heuristics to detect surface boundaries [9].

Second, *volume-oriented methods* consider the restrictive problem of reconstructing the closed surface bounding some solid. An early "volume sculpting" method was proposed by Boissonnat where various tetrahedra faces can be removed one by one [7], which was later refined in particular by Attali with a notion of r-regular shape taken from mathematical morphology [4]. Another variant, the *Power Crust,* is based on the power diagram (a weighted Voronoi diagram), with theoretical guarantees under a proper sampling assumption, and with polygonal interpolants rather than triangles [2]. The *tight cocone* is based on the original cocone method (see above), but specialized to produce a water-tight mesh for solids [11]. More recently, robustness to noise for this approach is based on a model where both the sampling density and noise level can vary locally [12].

[2]They could well be considered as a set of "hybrid" methods.

3. Surface Recovery via $\mathcal{MS}$ Transforms

We propose to reconstruct a surface mesh from unorganized point clouds by considering gap transforms on all A_1^3 shock curves in a rank-ordered greedy approach.[3] The greedy nature of the algorithm, in contrast to the ideal but impractical algorithm considering all sequences of gap transformations on the $\mathcal{MS}$, implies that local decisions in ambiguous cases may lead to erroneous results. Since the ranking is partially decided on the basis of a local surface neighborhood, these errors can then potentially propagate. To prevent the negative effects of such "local minima," we adopt a three-fold strategy. *(i)* The set of A_1^3 curves is divided into two distinct categories, based on whether the gap transform decision is categorically easy or difficult, leading to two passes of greedy iterations. The first pass aims at constructing valid surface triangles (*i.e.*, without ambiguity about their shape or local topology) in a greedy iterative sequence. Given a well-sampled input,[4] most surface triangles can be successfully built in this step. All remaining cases are then handled in the second pass, where the surface built in the first pass can be used to help resolve the initially ambiguous situations as discussed below. *(ii)* Since applying a gap transform can invalidate another candidate gap transform, in situations when a pair of gap transforms are close in ranking, *i.e.*, the difference in costs is such that $\delta\rho < \Delta_\rho$, their ranking is reduced by increasing their cost by a factor $\zeta > 1$, so as to delay a decision until additional local context is available.[5] *(iii)* A recovery option is available: after each gap transform, costs associated to neighbor surface interpolants (including already selected and candidate triangles) are re-evaluated: if the newly computed cost of a previously accomplished gap transform exceeds our top candidate's cost, we "undo" it by putting back the associated A_1^3 curve on a queue.

Initialization: The surface reconstruction is initialized by sorting A_1^3 curves into the two queues, $\mathbf{Q_1}$ and $\mathbf{Q_2}$ (for the 1st and 2nd greedy iterations). Each A_1^3 curve identifies three sample points, its *generators*, which can potentially be meshed neighbors on the original surface. Fig.7 shows the *three possible types* of candidate surface triangular interpolant. When there are no other sample points nearby the

[3]The A_k^n notation indicates the order (k) of contact of a maximal ball with n surface points. A_1^3 shock curves delimit A_1^2 $\mathcal{MA}$ sheets; for a point cloud, these curves are identically Voronoi edges, their A_1^4 endpoints are Voronoi vertices, and their duals are Delaunay triangles through the $n = 3$ sample/contact points. A_1^3 curves are computed from a sequence of critical points of the radius flow (the radius of maximal balls projected on the $\mathcal{MA}$): sources for $\mathcal{MA}$ sheets (A_1^2-2) are paired to find sources for shock curves (A_1^3-2), which in turn are paired to find A_1^4 endpoints; details in [19].

[4]We consider the theoretical sampling issues for our method elsewhere; the focus here is on introducing the algorithm for surface reconstruction and main philosophy behind the use of $\mathcal{MS}$ transitions.

[5]Experimentally, we have found that values of $\Delta_\rho = 5\%$ and $\zeta = 4\Delta_\rho$ lead to robust results; where "ρ" denotes a cost function.

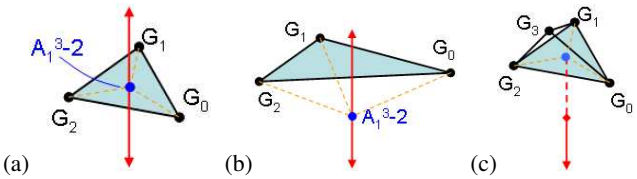

(a) (b) (c)

Figure 7. The three types of A_1^3 shock curves (red) and their corresponding Delaunay triangles (cyan) used in our method: (a) an A_1^3 curve with an *acute* triangle (type I), (b) an A_1^3 curve with an *obtuse* triangle (type II), (c) an A_1^3 curve not containing the $A_1^3{-}2$ critical point (type III).

three generators, the minimum-radius $\mathcal{MA}$ point for these 3 generators is always on the A_1^3 curve: it is the critical point of the radius flow, $A_1^3{-}2$, which sits at the circumcenter for the 3 generators and which is used to build the $\mathcal{MS}$ [19]. This critical point is then either inside (type I) or outside (type II) the interpolating (Delaunay) triangle, Fig.7.(a,b). Cases corresponding to types I and II are straightforward and used to create queue $\mathbf{Q_1}$. The remaining possibility of having the $A_1^3{-}2$ critical point not belonging to part of the A_1^3 curve indicates that a nearby forth generator is preventing its "formation" (*i.e.*, as being part of the $\mathcal{MS}$) and that the local connectivity is ambiguous (type III), Fig.7.(c). Cases corresponding to type III are more likely to lead to meshing ambiguities and are therefore used to create a separate queue $\mathbf{Q_2}$.

Rank ordering A_1^3 curves: The rank of each A_1^3 curve is based on *(i)* the likelihood that the corresponding triangle could have arisen from the original surface given the $\mathcal{MS}$ curve length,[6] and *(ii)* the consistency of the gap transform in reconstructing a surface given already neighboring meshed sample points. We discuss each case in turn.

Ranking A_1^3 curves *without* local context: Such a ranking can be decided on the basis of the shape and size of the candidate triangle with respect to the length of the $\mathcal{MS}$ curve. Let the sides of the triangle through 3 generators be d_1, d_2 and d_3, and the "length" of the A_1^3 curve, with respect to its $A_1^3{-}2$ critical point and for its shortest side, be R, and define:

$$\begin{aligned} D &= \max(d_1, d_2, d_3) \\ P &= d_1 + d_2 + d_3 \\ m &= (d_1 + d_2 - d_3)(d_3 + d_1 - d_2)(d_2 + d_3 - d_1) \\ A &= \sqrt{(P \cdot m)/16} \\ C &= 4\sqrt{3} \cdot A/(d_1^2 + d_2^2 + d_3^2)\,, \end{aligned}$$

where A is the triangle's area (Heron's formula) and C measures its compactness (Gueziec's formula). Then, the cost:

$$\rho_1 = \begin{cases} \frac{P}{R} \cdot \frac{1}{C^2}\,, & \text{if } D < d_{\max} \\ \infty\,, & \text{if } D \geq d_{\max} \end{cases}, \qquad (1)$$

favors compact triangles rather than elongated ones, and triangles smaller (w.r.t. D) than the length R of their associated A_1^3 curve; $d_{\max}$ represents the maximal expected triangle side length and is set in practice as: $d_{\max} = \eta \cdot d_{med}$, where d_{med} is the median of the histogram of $A_1^3{-}2$ radii of all type I and II shock curves (Fig.8).[7] Observe that this cost will delay the completion of triangles which are near corners and ridges in favor of those away from such "close encounters," a direct influence of the factor $1/R$ in eq. (1) (Fig. 9).

Ranking A_1^3 curves *with* local context: We now consider the relationship between an A_1^3 curve's putative surface triangle which can either share an *edge* or a *vertex* with its neighboring, already reconstructed surface triangles, Fig.10. First, a candidate triangle is more likely to

[6] Intuitively, an A_1^3 curve with a long side is more likely to approximate well the local normal field.

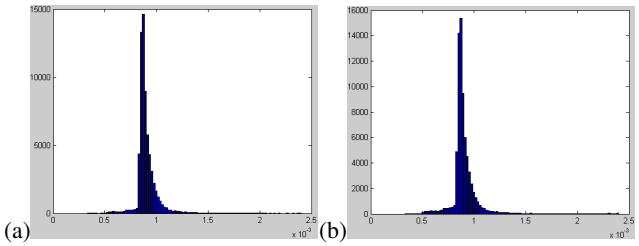
(a) (b)

Figure 8. (a) The distribution of the $A_1^3{-}2$ radii of all shock curves corresponding to triangles in the original mesh of the Stanford Bunny model. (b) The distribution of the $A_1^3{-}2$ radii of all shock curves of type I and II in the $\mathcal{MS}$ of the point cloud. Observe how the shape of the distributions resemble each other. The median of the $A_1^3{-}2$ distribution (d_{med}) is used to set $d_{\max}$ in eq.(1).

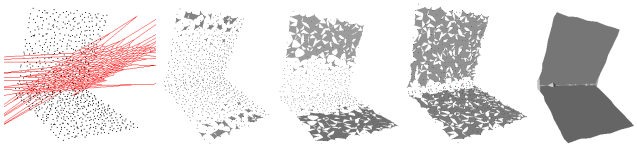

Figure 9. Steps in reconstructing a "corner shape" from 800 sample points which illustrate how our method favors meshing triangles in the region distant to the corner prior to meshing sharp features, where difficult decisions (due to under-sampling) have to be made. From Left to Right: the full $\mathcal{MS}$ (in red, with unbounded elements not shown); reconstructing the first 10%, 50%, and 90% of candidate triangles; final surface reconstruction result.

[7] d_{med} is used as the estimate of the expected *unit distance between samples*, while $5 < \eta < 15$ is a parameter which experimentally varies according to the sampling uniformity.

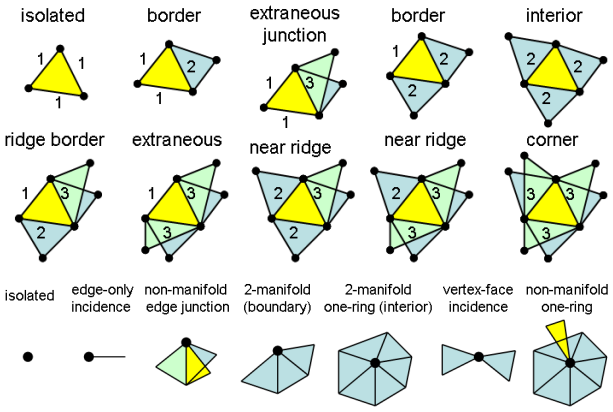

Figure 10. (Upper) Typology of mesh triangle topology based on simplicial adjacency at edges. (Bottom) Typology of mesh vertex topology based on its incident edges and faces.

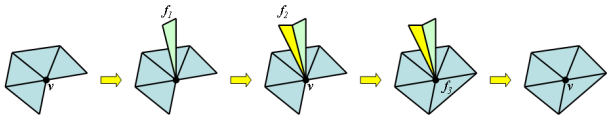

Figure 11. Schematic steps of meshing and fixing vertex topology dynamically in our meshing process to retain a "one-rinǵaround a vertex.

interpolate the surface if it is oriented similarly to its neighboring triangles, sharing an *edge* as determined by the dihedral angle θ between the two. When θ is small ($< 45°$) we expect the observed continuity to offset the cost ρ_1. When θ is large ($\geq 45°$) we expect the lack of continuity to rather augment the cost ρ_1. The function $f(\theta) = [\exp^{\theta} - 1]^2 - 1$ captures this notion well: at $\theta = 0$, $f(\theta) = -1$; at $\theta = 40°$, $f(\theta) \simeq 0$; at $\theta = 80°$, $f(\theta) \simeq 8.24$, giving us:

$$\rho_2 = \frac{d}{R} \cdot \frac{1}{C^2} \cdot f(\theta)\,, \qquad (2)$$

where d is the length of the shared edge. Thus, for a triangle with its three edges part of existing smooth surface patches, the contributions for ρ_2 add up to completely cancel ρ_1.

The second form of local context for a triangle is when it shares a *vertex* with an existing triangle. This is a locally ambiguous situation that can potentially lead to topological errors, Fig.10 bottom right, and must thus be delayed, avoided, or undone, to maintain a "one-ring" vertex topology, as described now in three possible cases. *(i)* If the shared vertex topology is already a *one-ring*, the new triangle should be rejected (Fig.10 bottom rightmost), since further meshing is unlikely to yield a better 2-manifold mesh with lower cost. *(ii)* If the shared vertex is a *vertex-face incidence*, (Fig.10 bottom second from right), the triangle should be delayed by increasing its cost and reinserted in in its queue to be considered later. *(iii)* If the shared vertex is a *non-manifold one-ring* (the second last of Fig.11), the *one-ring* topology will be recovered because the gap transforms will be undone as described earlier.

In summary, we mesh surfaces in a *best-first* manner considering the suitability of each candidate Delaunay triangle: it's shape, corresponding shock curve type and length, continuity from neighbors, and the local mesh topology. Our method is implemented as a multiple-pass greedy iterative algorithm. The first pass builds all confident surface triangles (with costs estimated via ρ_1 and ρ_2) from $\mathbf{Q_1}$; the second pass uses candidates from $\mathbf{Q_2}$ and resolves difficult cases using the local supports built from the first pass.[8]

Our method can further be fine-tuned when additional information is available. For example, each A_1^3 curve can be shown to robustly estimate a surface normal, a result related to Amenta *et al.*'s analysis of poles [1]; thus, when normals are available in conjunction with a point cloud, the candidate A_1^3 curve in the normal direction should be prioritized. When some existing mesh connectivity is already available, the local structure of the $\mathcal{MS}$ sharing such connectivity can be used to correctly select A_1^3 curves with associated (surface) triangles.

4. Experimental Results

We have implemented our method and extensively tested it in reconstructing surfaces with *various topologies*: closed (Fig.1.(c,f), 12, 13.(a,b,d), 15), with multiple components (Fig.6), non-orientable (Fig.1.(a)), multiply punctured (Fig.1.(b)), with multiple holes (Fig.13.(b), 15), closely knotted (1.(c), 13.(a)), with boundaries (Fig.1.(a,b,d,e), 6.(d), 9, 13.(c), 14, 17), and with sharp (discontinuous in curvature) ridges (Fig.1.(d,e), 9, 15, 17). [9]

In addition to meshing unorganized points, we point out two other useful applications: *(i)* re-meshing/repairing a partial mesh and *(ii)* handling very large inputs. First, we can re-mesh a partial mesh in two ways: either (a) by keeping all existing triangles known *a priori* to be correct and letting other candidate triangles compete to grow surface patches from these, or (b) by assigning high priority to existing triangles (in a *"polygon soup"*) over other new candidates and letting the algorithm re-mesh to a final surface set. Fig.14 validates our reconstruction result against the original model. Fig.1.(d) shows the result of *meshing raw data* from a single scan. Second, an important point not raised thus far is that since we have not imposed any strong restriction on the surface topology, we can handle *very large*

[8] Additional heuristics can be used *a posteriori* to fill remaining (large) holes if needed.

[9] Color scheme: all surfaces in "gold" are closed (water-tight) by our method; otherwise they are left in gray, with boundaries in blue.

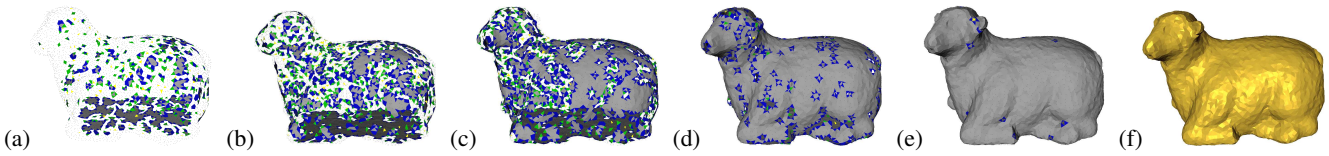

Figure 12. **Intermediate results of the 1st greedy iteration (for $22,619$ points sampling a sheep toy model) at (a) 10%, (b) 30%, (c) 50%, (d) 75%, (e) 90% completeness of the queue Q_1, which simulates an "inverse sampling" process as described in §1. Color scheme: in gray are shown "interior" triangles (Fig.10), in blue, triangles with 1 boundary side, and in green those with 2 boundary sides. (f) In this case, a water-tight surface is obtained after completion of the 1st greedy iteration.**

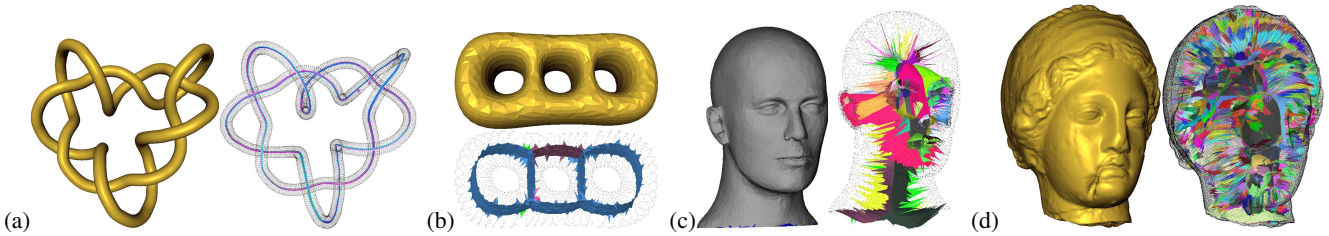

Figure 13. **Results of our reconstructed surfaces and corresponding $\mathcal{MS}+$'s. (a) Uniformly sampled knotted figure ($28,653$ points, $57,306$ faces, data from MPII). (b) Non-uniformly sampled triple donut shape ($1,996$ points, $3,999$ faces). (c) Cyberware Mannequin ($6,386$ points, $12,727$ faces); NB: not a solid, bottom is left open. (d) Cyberware Igea ($134,345$ points, $268,686$ faces).**

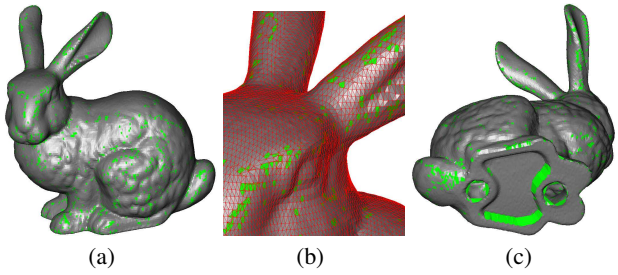

Figure 14. **Validation: Superimposing our resulting mesh on the Stanford Bunny shows that most of the original mesh is recovered. (a,b) The minor differences (green triangles) are the result of different triangulations of geometrically similar surface patches. (c) The narrow strips of holes at the bottom of the Bunny model are filled and the two larger circular holes are left unfilled in our result. Increasing η (and thus $d_{\max}$) would allow larger triangles to close these holes.**

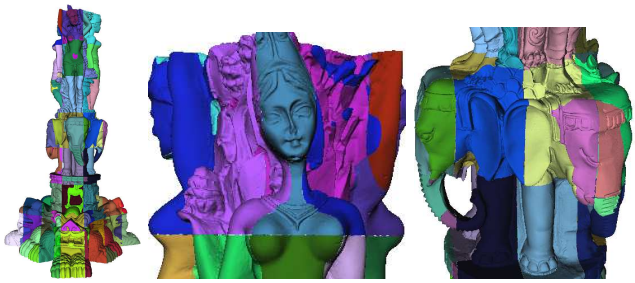

Figure 15. **Views of the reconstructed surface of the Stanford Thai Statue dataset ($\approx 5 \times 10^6$ points) using $7 \times 7 \times 7$ 3D bucketing.**

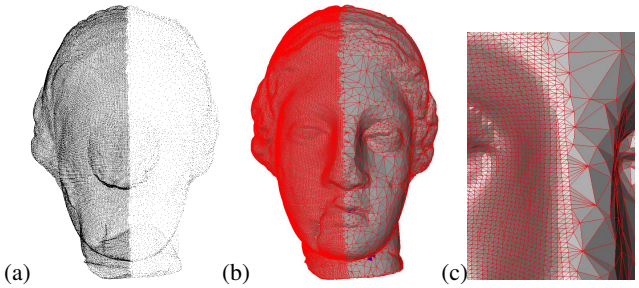

Figure 16. **(a) Igea dataset non-uniformly sampled with $75,545$ points (from MPII). (b) Our result made of $75,545$ vertices and $145,082$ faces. (c) Observe how our method preserve fine details on the densely sampled surface.**

datasets by simply dividing the space into 3D buckets and meshing surface within each bucket, Fig.1.(f) and Fig.15.[10] We can then stitch the surface pieces together to get a final model using the same algorithm *again*. Prior to stitching, we exclude the un-reliable triangles near bucket boundaries (*i.e.*, those which are built without support of nearby points from adjacent buckets). Then, the stitching of surfaces in adjacent buckets can be viewed as completing or repairing a partial mesh (by taking already meshed triangles near bucket boundaries as an initial solution).[11]

We have also tested our method for inputs made of *non-uniform* sampling as Fig.1.(c), Fig.13.(b,c) and Fig.16 demonstrate. The performance of our method degrades rea-

[10] We make use of an efficient way of constructing 3D buckets in the course of computing the $\mathcal{MS}$ as described by Leymarie & Kimia [19].

[11] Note also that the meshing of surfaces inside each bucket can be run in parallel, *e.g.*, on multicore architectures.

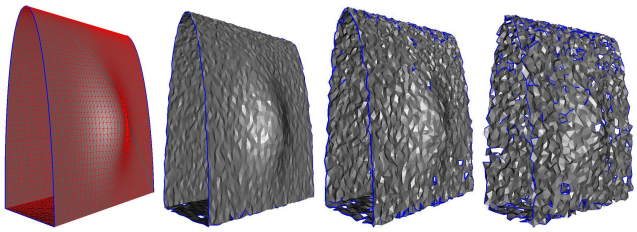

Figure 17. This figure shows how our method performs on inputs under perturbation w.r.t. d_{med}; Max. displacement $d_n = n \times d_{med}$, where n is a percentage; each point coordinate, x, y, z, is perturbed by a factor $h = rand \times d_n$, where $rand$ is a random number between $[-0.5, 0.5]$. Left to Right: original dataset ($8,014$ faces); 50% of noise ($11,196$ faces); 100% ($11,101$ faces); 150% ($11,018$ faces). Topological quality is initially reasonable and then degrades as the noise extent increases.

sonably as *perturbation* increases, Fig.17.

5. Conclusion

Our approach is capable of dealing with a great variety of surfaces whether they are closed or not, orientable or not, uniformly sampled or not. The current implementation is roughly as fast (and with pseudo-linear complexity in the number of samples) as other recent popular methods and the potential to handle vary large datasets is also very promising. We expect the capability of this approach to increase as additional $\mathcal{MS}$ transforms are included.

Acknowledgments: This material is based upon work partly supported by the National Science Foundation under Grants NSF/ITR-0205477 and NSF/KDI-BCS-9980091. The authors gratefully thank Gabriel Taubin and Peter Sibley for helpful early discussions. Thanks are also forwarded to Stanford graphics labs, Cyberware, and the Max Planck Institute for Informatics (MPII), for providing test scan data and some of the 3D models.

References

[1] N. Amenta and M. Bern. Surface reconstruction by Voronoi filtering. *Discrete and Comp. Geometry*, 22:481–504, 1999.

[2] N. Amenta et al. The power crust, unions of balls, and the medial axis transform. *IJCGA*, 19(2-3):127–153, 2001.

[3] N. Amenta et al. A simple algorithm for homeomorphic surface reconstruction. *IJCGA*, 12(1–2):125–1141, 2002.

[4] D. Attali. r-regular shape recons. from unorganized points. *Comp. Geom.: Theory & Applic.*, 10(4):239–247, 1998.

[5] F. Bernardini et al. The ball-pivoting algorithm for surface reconstruction. *IEEE Trans. on VCG*, 5(4):349–359, 1999.

[6] J. Blinn. A generalization of algebraic surface drawing. *ACM Transactions on Graphics*, 1(3):235–256, July 1982.

[7] J.-D. Boissonnat. Geometric structures for 3D shape representation. *ACM Trans. on Graphics*, 3(4):266–286, 1984.

[8] J. C. Carr et al. Smooth surface reconstruction from noisy range data. In *ACM GRAPHITE*, pages 119–126, 2003.

[9] D. Cohen-Steiner and F. Da. A greedy Delaunay-based surface recons. algorithm. *Visual Computer*, 20:4–16, 2004.

[10] B. Curless and M. Levoy. Volum. method for build. complex models. In *ACM SIGGRAPH*, pages 303–312, August 1996.

[11] T. K. Dey and S. Goswami. Tight cocone: A water-tight surface reconstructor. *JCISE*, 3(4):302–307, 2003.

[12] T. K. Dey and S. Goswami. Provable surface reconstruction from noisy samples. *Comp. Geometry*, 35:124–141, 2006.

[13] P. J. Giblin and B. B. Kimia. Transitions of the 3D medial axis. In *ECCV*, pages 718–724, 2002.

[14] P. J. Giblin and B. B. Kimia. A formal classification of 3D medial axis points. *PAMI*, 26(2):238–251, 2004.

[15] M. Gopi and S. Krishnan. A fast & efficient proj. based approach f. surf. recons. In *SIBGRAPI*, pages 179–186, 2002.

[16] H. Hoppe et al. Surface reconstruction from unorganized points. In *ACM SIGGRAPH*, pages 71–78, August 1992.

[17] J. Huang and C. H. Menq. Combinatorial manifold mesh recons. *Computer-Aided Design*, 34(2):149–165, 2002.

[18] B. B. Kimia, A. R. Tannenbaum, and S. W. Zucker. Shapes, shocks, and deformations, I. *IJCV*, 15(3):189–224, 1995.

[19] F. F. Leymarie and B. B. Kimia. The medial scaffold of 3D unorganized point clouds. *PAMI*, 29(2):313–330, 2007.

[20] C. T. Lim et al. Implicit reconstruction of solids from cloud point sets. In *3rd ACM Symp. on SMA*, pages 393–402, 1995.

[21] H.-W. Lin et al. A mesh reconstruction algorithm. *Computer-Aided Design*, 36(1):1–9, 2004.

[22] S. Muraki. Volumetric shape description of range data using "blobby model". *SIGGRAPH' 91,*, 25(4):227–235, 1991.

[23] Y. Ohtake et al. Sparse surface recons. with adaptive PU and RBF. *Graphical Models*, 68:15–24, 2006.

[24] S. Petitjean and E. Boyer. Regular and non-regular point sets. *Comp. Geom.: Theory & Applic.*, 19(2-3):101–126, 2001.

[25] M. Samozino et al. Recons. with Voronoi centered radial basis functions. In *Eurographics SGP*, pages 51–60, 2006.

[26] T. Sebastian, P. Klein, and B. Kimia. Recognition of shapes by editing their shock graphs. *PAMI*, 26:551–571, May 2004.

[27] A. Sharf et al. Competing fronts surface reconstruction. *Computer Graphics Forum*, 25(3):389–398, June 2006.

[28] D. Sharvit et al. Symmetry-based indexing of image databases. *JVCIR*, 9(4):366–380, 1998.

[29] G. Taubin et al. Param. families of polynom. for bounded algebraic curve & surface fit. *PAMI*, 16(3):287–303, 1994.

[30] H. Tek and B. B. Kimia. Boundary smoothing via symmetry transforms. *JMIV*, 14(3):211–223, May 2001.

[31] D. Terzopoulos and D. Metaxas. Dynamic 3D models. *PAMI*, 13(7):703–714, July 1991.

[32] H.-K. Zhao et al. Fast surf. recons. using the level set method. In *IEEE Wksh. VLSM*, pages 194–202, 2001.